Arecibo S-band Radar Characterization of Local-scale Heterogeneities within Mercury's North Polar Deposits

Rivera-Valentín, Edgard G.

2022-03-14

Arecibo *S*-band Radar Characterization of Local-scale Heterogeneities within Mercury's North Polar Deposits

Edgard G. Rivera-Valentín[1] , Heather M. Meyer[2] , Patrick A. Taylor[1,8] , Erwan Mazarico[3] , Sriram S. Bhiravarasu[4] ,
Anne K. Virkki[5,9] , Michael C. Nolan[6] , Nancy L. Chabot[2] , and Jon D. Giorgini[7]

[1] Lunar and Planetary Institute, Universities Space Research Association, 3600 Bay Area Boulevard, Houston, TX 77058, USA; rivera-valentin@lpi.usra.edu
[2] Johns Hopkins University Applied Physics Laboratory, Laurel, MD 20723, USA
[3] NASA Goddard Space Flight Center (GSFC), Greenbelt, MD 20771, USA
[4] Space Applications Centre, Indian Space Research Organization, Ahmedabad, India
[5] Arecibo Observatory, University of Central Florida, Arecibo, PR 00612, USA
[6] University of Arizona, Lunar and Planetary Laboratory, Tucson, AZ 85721, USA
[7] Jet Propulsion Laboratory, California Institute of Technology, Pasadena, CA, USA

Abstract

Ground-based planetary radar observations first revealed deposits of potentially nearly pure water ice in some permanently shadowed regions (PSRs) on Mercury's poles. Later, the MESSENGER spacecraft confirmed the icy nature of the deposits, as well as their location within PSRs. Considering the geologic context provided by MESSENGER, we further characterized the north polar deposits by pairing spacecraft data with new Arecibo *S*-band radar observations. Here we show that some ice deposits within PSRs have a gradational pattern in their radar properties that is likely associated with differences in ice purity. Radar-bright features with a circular polarization ratio $\mu_c > 1$ can be characterized by water ice with $\gtrsim 3\%$ impurities by volume while those with $\mu_c < 1$ by $\gtrsim 20\%$ impurities. Furthermore, areas in PSRs with $\mu_c < 1$ typically surround locations of stronger radar backscatter with $\mu_c > 1$. Therefore, deposits of nearly pure water ice are likely surrounded by lower-purity material, such as water-ice-rich regolith, which could be the result of impact gardening or the crater's thermal environment. However, such deposits are not always colocated within large polar craters where ice should be the most stable, even at the surface. In fact, we found that there is no significant difference between the radar backscattering properties of deposits thought to have surficial ice and those with buried ice. Our results also help improve the identification of icy reservoirs elsewhere, such as the Moon. Indeed, we found that μ_c is not an adequate diagnostic, but rather the radar backscatter in each circular polarization independently provides information to identify water-ice deposits.

Unified Astronomy Thesaurus concepts: Mercury (planet) (1024); Radar astronomy (1329); Planetary polar regions (1251); Surface ices (2117)

1. Introduction

After the determination of Mercury's rotation rate (Pettengill & Dyce 1965), another notable ground-based, radar-enabled discovery was the identification of radar-bright features at its poles (Harmon & Slade 1992; Slade et al. 1992). These features are distinguishable from the background terrain by their high radar albedo and circular polarization ratio similar to those observed from icy moons (Harmon et al. 1994, 2001). Modeling suggested the radar backscatter occurred from a low-loss volatile, such as clean water ice (Hapke 1990; Slade et al. 1992; Butler et al. 1993). These anomalous radar-bright features appeared to be confined to the interior of impact craters, suggesting a potential volatile reservoir in areas shaded from direct sunlight by local topography (i.e., permanently shadowed regions or PSRs) (Harmon et al. 1994). Indeed, thermal models of Mercurian polar craters predicted stable water ice in such PSRs within some $10°$ of the pole and at

lower latitudes if insulated by a thin layer (Paige et al. 1992; Vasavada et al. 1999). Later, the MESSENGER spacecraft confirmed that radar-bright features are typically associated with PSR locations (Chabot et al. 2012; Deutsch et al. 2016) and that the northern polar region of Mercury is on average hydrogen rich in comparison to lower latitudes (Lawrence et al. 2013).

MESSENGER data further revealed, based on local cratering and topography, that the putative ice deposits may be a few meters thick (Eke et al. 2017; Deutsch et al. 2018; Rubanenko et al. 2019; Susorney et al. 2019) and may have been emplaced within the last 300 Ma (Deutsch et al. 2019). Thermal models informed from MESSENGER-derived topography predict that the maximum surface temperatures within the "big five" north polar craters—Prokofiev, Kandinsky, Tolkien, Tryggvadóttir, and Chesterton—would be low enough, $\lesssim 110$ K, to permit stable surface water ice (Paige et al. 2013; Chabot et al. 2018a). This prediction has been supported by images from MESSENGER's Wide-Angle Camera (WAC) and reflectance measurements from the Mercury Laser Altimeter (MLA) instrument, which suggest exposed surface ice within these craters (Chabot et al. 2014, 2016, 2018a; Deutsch et al. 2017). However, the circular polarization ratio and radar albedos of all of these craters are higher in the *S* band (12.6 cm, 2380 MHz) than in the *X* band (3.5 cm, 8560 MHz), which could be interpreted as the existence of a few-centimeter-scale scattering layer, as

---

[8] Now at National Radio Astronomy Observatory, 1180 Boxwood Estate Road, Charlottesville, VA 22903, USA, Green Bank Observatory, P.O. Box 2, Green Bank, WV 24494, USA.
[9] Now at University of Helsinki, Helsinki, 00014, Finland.

would be expected from mantling by a thin dust layer (Harcke [2005](#); Harmon et al. [2011](#)). Indeed, measurements with MESSENGER's Mercury Dual Imaging System (MDIS) and MLA showed that the majority of radar-bright features in PSRs outside of the big five north polar craters were optically darker than the surrounding terrain, indicating that these ice deposits are buried beneath a low-reflectance, perhaps organic-rich, material (Neumann et al. [2013](#); Chabot et al. [2014](#), [2016](#), [2018a](#); Hamill et al. [2020](#)).

Furthermore, Deutsch et al. ([2016](#)) found that many PSRs at the north pole lack a significant Arecibo *S*-band radar return, and Chabot et al. ([2018b](#)) found the same for the south polar region. That some PSRs lack significant radar backscatter may suggest that not all cold traps are occupied by water ice, which could provide constraints on the timing and amount of volatile delivery to the Mercurian poles. Alternatively, thin water ice deposits that do not cause a strong radar return, as well as deeply buried deposits beyond the radar penetration depth, can also explain the discrepancy. Data from MESSENGER's Neutron Spectrometer, though, suggest that on average water ice in Mercury's north pole is only buried beneath a hydrogen-poor layer 10–20 cm thick (Lawrence et al. [2013](#)), which is very shallow compared to the *S*-band penetration depth (the reader is referred to Section [3](#) for a detailed discussion of radar penetration depth). Another option is that PSRs without radar-bright features were not sampled by radar observations due to the local incidence angle. High-resolution MESSENGER topography can help resolve this latter option.

In fact, the wealth of geologic and compositional information provided by the MESSENGER mission provides excellent context to improve interpretations from radar studies. Ground-based planetary radar observations provide constraints on the near-surface, centimeter-to-meter-scale regolith properties of planetary bodies; however, scattering of the radar signal is impacted simultaneously by the physical properties of the scatterers (e.g., their geometry, size, and shape distribution) and the bulk dielectric properties of the unit (e.g., Virkki & Muinonen [2016](#)). Orbital-based, high-resolution observations provide important context to help resolve the physical properties resulting in the radar scattering, allowing for improved characterization of planetary surfaces down to the penetration depth of the radar.

Here, we report on the analysis of the first ground-based radar observations of Mercury acquired since the end of the MESSENGER mission, taking advantage of its extensive and rich data set for context. Given the high-resolution MESSENGER topographic maps of the north pole, we simulated the radar incidence angle at the same resolution as the radar images. This enabled us to use radar-scattering models to study the differences in the properties of the polar-bright features and the background terrain, providing new constraints on the purity of the icy polar deposits. Additionally, we studied variations in the radar backscatter within PSRs to improve the interpretation of intercrater differences.

2. Radar Observations

We conducted radar observations for six days around the 2019 inferior conjunction, which occurred on 2019 July 21, using the Arecibo Observatory *S*-band (12.6 cm, 2380 MHz) planetary radar system. Mercury is closest to Earth near inferior conjunction, which in 2019 was at 0.576 au, thereby maximizing the signal-to-noise ratio (S/N) of radar images. During an

observing run at Arecibo, a modulated circularly polarized beam of light was transmitted for the time it takes light to reach and return from Mercury (i.e., the round-trip time, RTT). The returned echoes are then received for the same time in both the same-circular (SC) and opposite-circular (OC) polarization as transmitted. During a single day, tracks were nominally 2.75 hr long permitting up to eight transmit–receive cycles (or runs). The subradar latitude during the six-day observing campaign ranged from $11°\!.4$N to $11°\!.6$N, and the subradar longitude ranged from $303°\!.9$W to $338°\!.5$W. A summary of observing parameters for the six-day observing campaign is shown in Table [1](#). Because of the northern subradar latitude, only the north polar region was observable. The next inferior conjunction that leads to southern subradar latitudes, and thus a favorable opportunity to study Mercury's southern polar deposits, will be in 2024 April 15 when the subradar latitude will be $4°\!.8$S.

Because the antenna beamwidth at the *S* band ($\sim2'$) is much larger than Mercury's angular width ($\sim0'\!.2$), only full-disk observations are possible, which means the north–south ambiguity is unavoidable (Ostro [1993](#)). Delay-Doppler images are radar backscatter maps in delay (range) and Doppler (frequency) space. For a rotating spherical object, areas within annuli centered at the subradar point map to the same range value, while points within semiannuli centered at the approaching/receding limbs map to the same frequency value. Annuli of isorange and isofrequency values thus intersect twice, once in each hemisphere, north and south of the Doppler equator. This means that a pixel in delay-Doppler space corresponds to backscatter from conjugate points. In this work, we focus only on the northern polar terrain where, due to the northern subradar latitude, the expected dominant backscatter should be from the northern polar deposits, while latitudes south of $\sim78°\!.5$S should not be visible (i.e., where the south polar deposits lie).

Our observations were conducted after Hurricane Maria, which devastated Puerto Rico and damaged the Arecibo telescope in 2017 September. At the time of the reported observations, the maximum transmitted power was halved to roughly <400 kW because only one klystron amplifier was in operation. Furthermore, the telescope's gain was reduced to 7 K Jy^{-1}, compared to 10 K Jy^{-1} before Hurricane Maria, due to damage and misalignment of the reflecting surface. The telescope's gain was also a function of azimuth and zenith angle and was lower on the east side of the dish. Additionally, technical issues with the low-noise amplifiers resulted in increased thermal noise in the OC channel. In addition to reduced gain, the telescope-pointing accuracy at the edge of the dish was also affected for post-Maria observations. Here, only runs that started away from the edge of the dish, when Mercury had risen higher in Arecibo's field of view, are analyzed. Even with all of that, Arecibo's sensitivity remained unsurpassed, so our observations resulted in a full-disk matched filter S/N $\geqslant 300{,}000$ per day (i.e., summed over the eight possible daily runs), far higher than any other ground-based radar system in any configuration.

2.1. Dual Polarization Delay-Doppler Imaging

Radar images were generated using the long-code method described in Harmon ([2002](#)), which we briefly summarize here. Due to Mercury's size and rotation period, it is an overspread radar target leading to Doppler aliasing, which appears as a

Table 1
Arecibo S-band Radar Observations of Mercury during the 2019 Inferior Conjunction

UT Date yyyy-mm-dd	RTT (s)	P_{tx} (kW)	Runs	Subradar Latitude (°N)	Subradar Longitude (°W)
2019-07-19	576	392	5	11.52	303.88–304.65
2019-07-20	578	342	2	11.56	310.68–311.45
2019-07-21	582	371	6	11.57	317.48–318.26
2019-07-22	586	389	6	11.54	324.28–325.04
2019-07-23	592	391	4	11.48	331.04–331.81
2019-07-24	599	348	4	11.40	337.77–338.54

Notes. UT Date is the universal-time date on which the observation began. RTT is the round-trip light time to the target. P_{tx} is the transmitter power. Runs is the number of completed transmit–receive cycles that were used in this study.

folding of the target in the frequency dimension in radar images. To compensate, Harmon (2002) developed the long-code method, which eliminates Doppler aliasing of the overspread echoes but introduces self-clutter noise. For Mercury, the self-clutter noise is negligible in the SC ($\sim$5%) and modest in the OC ($\sim$30%) polarization (Harmon 2002; Harmon et al. 2011). We conducted observations by transmitting a binary-phase-coded radar signal with a 10 μs baud, which results in a resolution of 1.5 km pixel^{-1} along the delay axis in radar images. However, this range resolution projected onto the surface of the planet is a function of the radar incidence angle. For a perfectly smooth, topography-free sphere, delay depth in a radar image is related to the radar incidence angle as

$$\phi = \cos^{-1}\left(1 - \frac{tc}{2R}\right), \qquad (1)$$

where t is the echo delay-depth relative to the spin pole. The range resolution projected onto the surface in our experiments is then $\dfrac{1.5}{\sin(\phi)}$ km pixel^{-1}, such that at $\phi \sim 50°$, the resolution is 2 km (Campbell 2002). The frequency of the transmitted signal is compensated for the Doppler shift due to the relative motion between Arecibo and Mercury such that the echo from the subradar point on Mercury returned to Arecibo centered at 2380 MHz (plus a nominal constant transmit offset). During the receive cycle, echoes were sampled at twice the baud rate, which results in twice as fine pixel spacing in the delay axis. The Doppler resolution was processed to 0.238 Hz, which results in a transverse mapping resolution of 1.1 km. In one RTT, the apparent rotation of Mercury results in smearing across 0°.05 in longitude (i.e., 0.37 km at 80°N and 2.1 km at the subradar latitude). Thus, in the northern polar regions, the smearing is lower than the pixel size, while at the leading edge of the echo, it results in smearing over two pixels.

Each delay-Doppler image was first calibrated against system noise by removing a flat baseline fit to the Doppler spectra from the echo-free delays. Images were then calibrated against self-clutter noise, which results as echo power from unsynchronized delays are added as random, noise-like clutter in other delay bins (Harmon 2002). The total power in noise-only bins was found along the frequency dimension, spread evenly over the delay depth, and then removed from the echo at the corresponding frequency bin. These calibration steps were taken for every run. After system and self-clutter noise correction, delay-Doppler images in each polarization for every

run were normalized to units of radar cross-sectional area. Thus, the sum of the final run products result in the total radar cross section for Mercury, which has a full-disk OC and SC radar albedo of $\hat{\sigma}_{\text{OC}} = 0.06$ and $\hat{\sigma}_{\text{SC}} = 0.005$ (Harmon 1997), such that, e.g., the full-disk OC radar cross section is $\sigma_{\text{OC}} = \hat{\sigma}_{\text{OC}}(\pi R^2)$, where $R = 2439.7$ km is Mercury's radius. The whole-disk OC radar albedo of Mercury varies little with subradar point, from $0.04 \leqslant \hat{\sigma}_{\text{OC}} \leqslant 0.08$, indicative of a surface globally dominated by porous, unconsolidated regolith (Harmon & Campbell 1988).

In Figure 1, we show an example delay-Doppler image from observations on 2019 July 19. The image shows the total backscatter power in both OC and SC polarizations over all the runs of that day. In Figure 1, we separately plot the OC and SC radar cross-section density as a function of delay, such that the integral of the function is the full-disk OC and SC radar cross section, respectively. Backscatter in the OC polarization is dominated by strong quasi-specular reflections at the leading edge. By a delay of 2000 μs (i.e., $\phi \sim 30°$), radar backscatter has sharply fallen by two orders of magnitude, demonstrating the transition to the diffuse scattering regime. After a delay of 10,000 μs (i.e., $\phi \sim 70°$), the radar cross-section density in the OC and SC polarizations is similar. Over the poles, the high SC radar backscatter associated with the deposits can be seen as the SC radar cross-section density exceeds OC values (e.g., $\sim$13,000, or $\sim$80°).

Additionally, Figure 1 shows several notable features in the radar image. The radar-bright features at the pole stand out (near 12,000 μs in delay), almost rivaling the bright, leading edge despite the oblique/grazing incidence angle ($\phi \sim 75°$). Additionally, several small bright features are seen halfway in the echo ($\sim$8000 μs), which would correspond to the polar deposits near 70°N. Several craters are discernible near the leading edge with bright radar reflections caused by scattering off of radar-facing facets. Among these, there is a multiring feature at the center of the leading edge (0 Hz, 700 μs), which is the 290 km diameter Rachmaninoff crater (27°.7N, 302°.6W). The smooth interior of Rachmaninoff is readily notable as relatively radar dark, resulting from scattering off of the interior smooth plains, which may be impact melt and/or volcanism (Prockter et al. 2010). On the left of the image (-30 Hz, 4200 μs) a circular radar-bright feature is discernible in the echo. This high radar backscatter is likely a result of the blocky continuous ejecta of the fresh 29 km diameter rayed crater Fonteyn (32°.8N, 264°.4W), as was found for other rayed Mercurian craters (Neish et al. 2013).
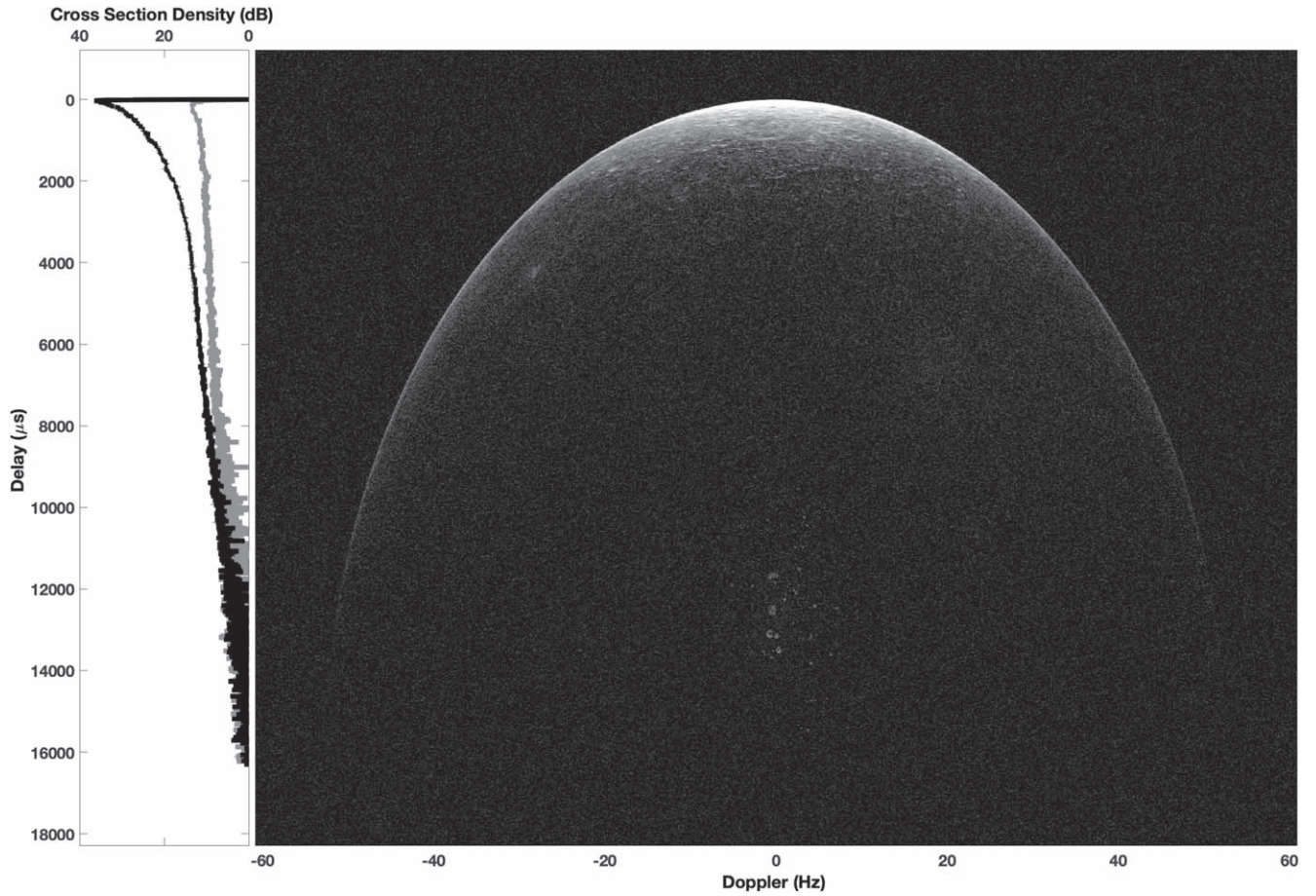
Figure 1. *S*-band delay-Doppler image of Mercury from 2019 July 19 as total OC and SC backscatter with pixel values in units of standard deviations above the noise baseline (i.e., linear *z*-scores). The color map is clipped such that *z*-scores < 0 map to black and *z*-scores > 100 map to white. On the left, we plot the OC (black) and SC (gray) radar cross-section density in units of dB (i.e., logarithmic) as a function of delay in units of μs.

2.2. Projection to Hermiocentric Coordinates

Using ephemeris-derived values for Mercury's Doppler bandwidth, the Doppler angle, which is the angle between the true and apparent spin axis, and subradar points during every run, the corresponding hermiocentric position was calculated for every pixel from its delay-Doppler coordinates following standard methods (Pettengill et al. 1974; Campbell 2002; Campbell et al. 2007), which we briefly summarize here. The frequency and range of every Mercury echo pixel were used to calculate the corresponding latitude (θ) and longitude (φ) on a sphere. If the subradar point is at $\theta = 0°$ and $\varphi = 0°$, then

$$\varphi = \tan^{-1}\left(\frac{f\lambda}{(2R - tc)\pi\omega}\right), \qquad (2)$$

where f is Doppler frequency, λ is the transmitted wavelength, and ω is the inverse of the apparent rotation period, and

$$\theta = \cos^{-1}\left(\frac{\cos\phi}{\cos\varphi}\right). \qquad (3)$$

Because the subradar point was not centered at (0°N, 0°W), the hermiocentric coordinate system with respect to the observer has undergone a transformation in pitch and roll, described by a rotation matrix. A transformation in pitch accounts for the shift in latitude and roll accounts for the shift in longitude to the

subradar point. The calculated latitude and longitude are converted to Cartesian coordinates (x, y, z), which are then transformed in pitch as

$$\begin{bmatrix} x_p \\ y_p \\ z_p \end{bmatrix} = \begin{bmatrix} x \\ y \\ z \end{bmatrix} \begin{bmatrix} \cos(-\theta_r) & 0 & \sin(-\theta_r) \\ 0 & 1 & 0 \\ -\sin(-\theta_r) & 0 & \cos(-\theta_r) \end{bmatrix}, \qquad (4)$$

where θ_r is the subradar latitude. These points are then transformed once more in roll as

$$\begin{bmatrix} x_r \\ y_r \\ z_r \end{bmatrix} = \begin{bmatrix} x_p \\ y_p \\ z_p \end{bmatrix} \begin{bmatrix} 1 & 0 & 0 \\ 0 & \cos(\gamma) & -\sin(\gamma) \\ 0 & \sin(\gamma) & \cos(\gamma) \end{bmatrix}, \qquad (5)$$

where γ is the Doppler angle, defined as positive clockwise, which orients the *z*-axis to match Mercury's apparent spin axis during each run. These transformed Cartesian points are then converted to spherical coordinates to obtain the pixel's true latitude and longitude. These points are then mapped onto a polar stereographic grid with a center latitude and longitude of 90°N and 0°W, respectively, only for points >60°N.

A radar backscatter coefficient (σ^0) map in polar stereographic projection per run is then produced by dividing the radar cross-sectional area by the illuminated area per pixel. The final campaign radar backscatter coefficient map for each polarization is a weighted average over all runs. The weights

Table 2
Comparison against Previous Observations

Crater	Center Location	μ_c This Work	μ_c Harmon et al. (2011)
Prokofiev (K)	85°7N, 297°1W	1.38	1.31
Kandinsky (J)	87°9N, 281°2W	1.43	1.40
Tolkien (H)	88°8N, 211°1W	1.45	1.42
Tryggvadóttir (E)	89°6N, 171°6W	1.43	1.44
Chesterton (D)	88°5N, 126°9W	1.53	1.46
Petronius (M)	86°1N, 40°5W	1.45	1.36
Remarque (N)	84°9N, 6°5W	1.40	1.31

Notes. Comparisons are made against the reported values in Table 2 of Harmon et al. (2011). As a guide, the Harmon et al. (2011) index for the craters is provided in column 1 in parentheses after the crater's name. Our values for μ_c are averages over the crater's radar-bright features.

are derived as the pixel's z-score relative to the average noise in echo-free pixels of every run. Radar images are typically z-score normalized such that the sum of echo-free pixels is zero, their standard deviation is one, and all pixels are represented by the raw value's distance from the mean noise baseline in units of standard deviation. As such, positive z-scores represent how confident the pixel value is above the noise. Here, we conducted the weighting only over pixels with a z-score > 0 (i.e., the pixel was above noise); otherwise, a flat average was taken if a map location consistently across all runs had a z-score < 0 (i.e., below system noise). A circular polarization ratio (μ_c) map was also produced by dividing the final campaign σ_{OC}^0 and σ_{SC}^0 maps and μ_c calculated only for values whose z-score was above the background noise in both polarizations. Final campaign radar maps were referenced against a MESSENGER MDIS map of the north polar terrain by using the calculated pixel latitude and longitude. Using feature matching, the radar maps were found to require on average an adjustment on the order of 1 km (i.e., 1 pixel) to best match features within latitudes $>60°$N.

Uncertainty in radar cross-section values are primarily due to systematic calibration, which is typically $\sim 20\%$, while uncertainty in the circular polarization ratio is smaller, $\sim 5\%$–10%, because the systematic calibration errors largely cancel out (Ostro 1993; Harmon et al. 2011; Nolan et al. 2013). Here, to validate the radar maps, our measured μ_c was compared against the reported values in Harmon et al. (2011) for Prokofiev, Kandinsky, Tryggvadóttir, Tolkien, Chesterton, Remarque, and Petronius. As can be seen in Table 2, values are similar within error.

In Figure 2, we show the resultant campaign σ^0 map in the SC polarization for latitudes $>75°$N. We note that unlike in Harmon et al. (2011), we do not plot here the equivalent full-disk radar albedo to avoid assumptions of the underlying scattering law. Furthermore, when comparing Figure 2 to earlier maps, recall that earlier maps were sums of multiyear campaigns from 1999 to 2005. Even then, although our radar map lacks some of the finer details in Harmon et al. (2011), it is largely consistent with those earlier observations.

2.3. Identification of Radar-bright Features

In previous work, radar-bright features were identified by setting a z-score floor (i.e., by setting all values below a z-score threshold to black to concentrate only on the highest radar backscatter). However, this can obscure important features,

such as gradation of radar backscatter potentially associated with ice purity. Here, to facilitate analysis of the radar-bright polar features shown in Figure 2, we applied a density-based clustering algorithm to automate their identification. We used DBSCAN, or Density-Based Spatial Clustering of Applications with Noise (Ester et al. 1996), which identifies clusters of like signals in large data sets with noise. DBSCAN is an unsupervised machine-learning algorithm dependent on three parameters: the threshold distance between points of like signal strength such that they can be considered neighbors (η), the minimum number of neighboring points required to identify a cluster, and the distance metric (i.e., Euclidean). The choice of η is optimized by finding the average distance of each mapped point to at least 20 nearest neighbors of similar signal strength, plotting these results in ascending order, and finding the point of maximum curvature (Rahmah & Sukaesih Sitanggang 2016), which resulted in $\eta = 5$. The method adequately automatically identified the radar-bright features. Some small, seemingly radar-bright features, including the diffuse patch, which is an area of unresolved brightness that appears between the Kandinsky and Tryggvadóttir craters (Harmon et al. 1994), were not identified by this technique.

In Figure 3, we show an overlay of the DBSCAN-identified radar-bright features on a MESSENGER MDIS map. Additionally, Figure 3 denotes PSRs within craters as constrained by MESSENGER. We find that all radar-bright features identified by DBSCAN lie within a PSR, consistent with previous conclusions (Deutsch et al. 2016). Although there are some small areas that are identified as radar bright but not within a PSR, these are typically one or two pixels outside of a PSR. These are likely due to pixels that represent areas partially occupied by ice, uncertainties in georeferencing, and/or an artifact of the DBSCAN procedure. Furthermore, as has already been shown (e.g., Deutsch et al. 2016), many PSRs lack a radar-bright feature. Several midsized craters, such as Sapkota (86°1N, 132°8W) and Burke (85°9N, 171°6W), are not associated with a significant cluster of high radar albedo. We note that for these craters no significant radar-bright feature was also identified within the maps of Harmon et al. (2011), which are a composite of observations over subradar longitudes from 11°W to 349°W.

3. Analysis of Radar Scattering

Regolith properties, such as density, composition, and particle size distribution, alter how the incident radar beam scatters from the surface. Typically, radar scatters off of wavelength-scale structures (e.g., topography, boulders, etc.). At low incidence angles, OC echoes result from specular, single-scattering events from the surface while at high incidence angles OC echoes primarily result from diffuse scattering, such as rocks (Ostro 1993; Black 2002). As seen in Figure 1, the transition to diffuse scattering begins to occur on Mercury for $\phi \sim 30°$ and OC and SC backscatters are similar for $\phi \gtrsim 70°$. On the other hand, SC echoes result from diffuse scattering at all incidence angles. For the high-incidence polar terrains studied here, both the OC and SC echoes primarily occur from diffuse scattering.

Additionally, a radar experiment samples into a planetary regolith to a depth characterized by the material's dielectric permittivity, such that after traveling a distance (d) in the regolith, the wave is attenuated by a factor of $e^{-\beta d}$, where β is
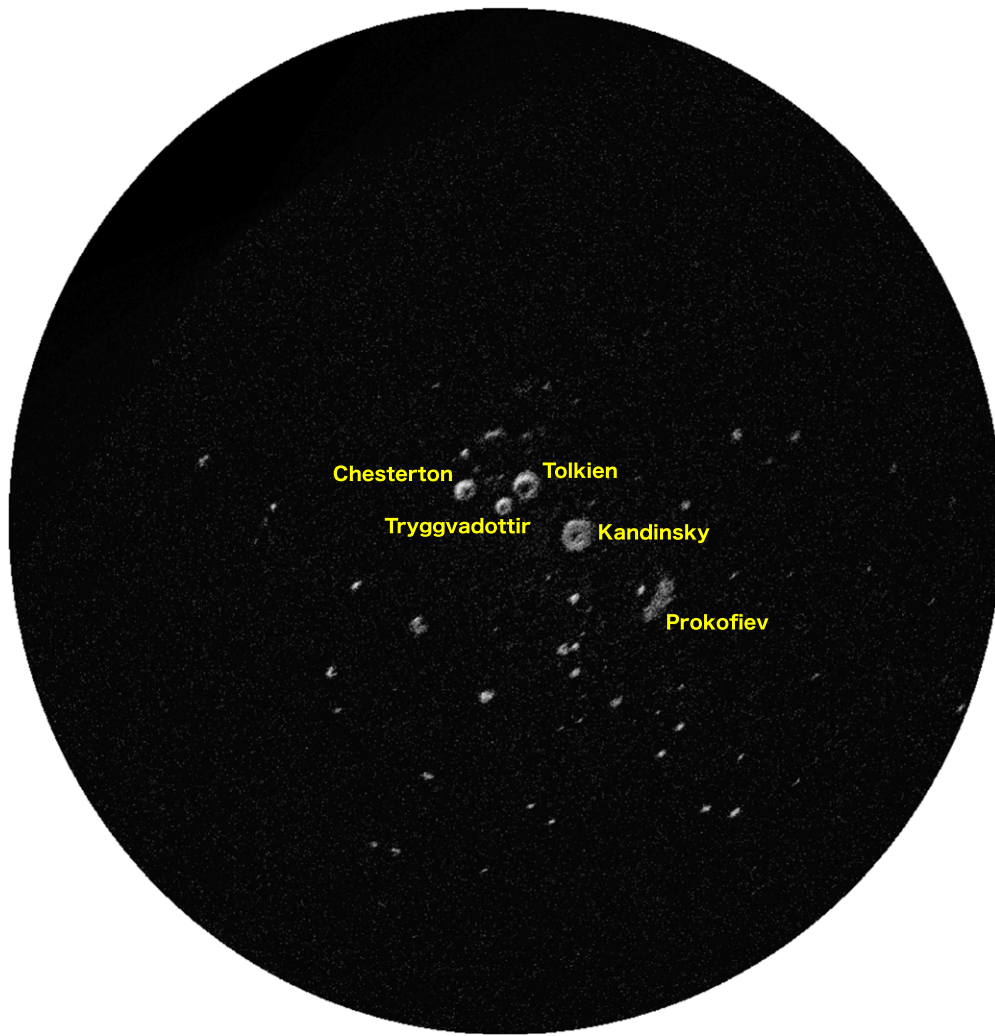
Figure 2. SC radar backscatter coefficient map of the northern terrains in polar stereographic projection generated over the six-day observing campaign. Radar backscatter is in units of z-score. The map is limited to latitudes >75°N. The "big five" craters in the area, Prokofiev, Kandinsky, Tolkien, Chesterton, and Tryggvadóttir, are labeled in yellow.

the absorption coefficient and is defined as

$$\beta = \frac{2\pi\epsilon_i}{\lambda\sqrt{\epsilon_r}}, \qquad (6)$$

where $\epsilon = \epsilon_r - i\epsilon_i$ is the complex dielectric permittivity, which describes the response of a material to an electric field in both magnitude and phase (Black 2002). The e-folding distance ($1/\beta$) is typically considered because the radar wave is attenuated by a total of e^2 as it travels this distance and back again. The sampled depth normal to the planetary surface over the e-folding distance is reduced by the incidence angle as $\cos\phi$ such that it is maximized at the subradar point. As such, returned echoes are affected by the bulk sampled regolith composition.

Commonly, a basalt analog is used for planetary radar studies. The dielectric permittivity of solid basalt is $7.7 - i0.2$, while that of powdered, porous basalt is reduced to $\epsilon \sim 3 - i0.02$ (Campbell & Ulrichs 1969). Indeed, Heggy et al. (2020) has derived $2.3 < \epsilon_r < 3.8$ for lunar regolith fines associated with craters of varying sizes using measurements from the Mini-RF radar instrument aboard the Lunar Reconnaissance Orbiter. The expected sampled depth, normal

to the surface, by the radar beam for lunar-like material is then $1/\beta = 1.7$ m at $\phi = 0°$ and $1/\beta = 0.3$ m at $\phi = 80°$ in the S band. Although the real component of the dielectric permittivity of water ice is comparable to porous basalt, the imaginary component is far smaller, resulting in $\epsilon = 3.2 - i0.001$ (Matzler & Wegmuller 1987). Thus, the expected sampled depth normal to the surface for a radar beam incident on water ice is much larger, 35 m and 6 m for $\phi = 0°$ and $80°$, respectively. This can lead to multiple scattering events from heterogeneities within the ice that add up coherently, i.e., the coherent backscatter opposition effect (CBOE) (Hapke 1990; Hapke & Blewett 1991). CBOE is thought to be responsible for the high radar backscatter coefficients and circular polarization ratios common to the icy moons of Jupiter (Campbell et al. 1977; Ostro et al. 1992; Black et al. 2001).

Here, we sought to characterize the ice purity and wavelength-scale properties of the radar-bright features. We used modeling of radar scattering to compare the properties of the background terrain to radar-bright features. These differences inform the best diagnostic tools to identify subsurface ice, as well as constrain the material properties.
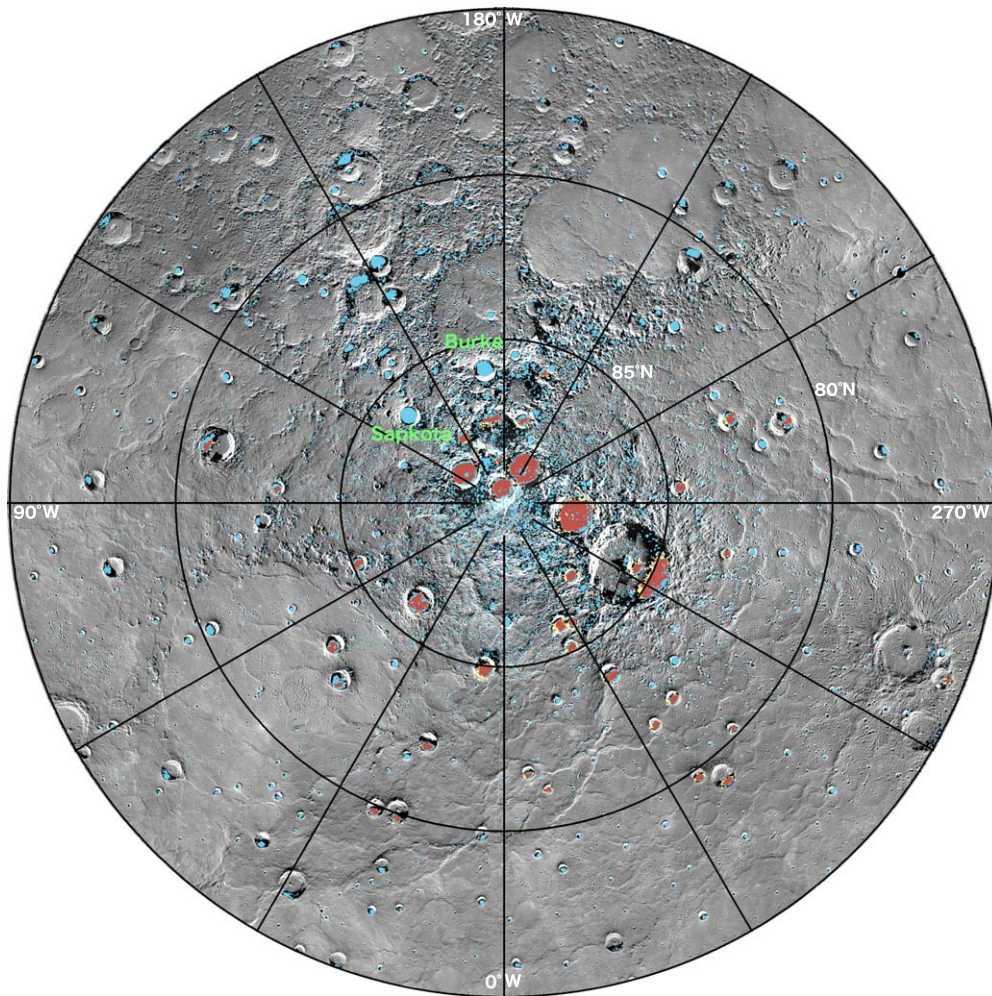
Figure 3. Overlay of the DBSCAN-identified radar-bright features (yellow) onto a MESSENGER MDIS map of the northern polar terrain. In cyan, we show the MESSENGER-constrained locations of areas within craters that are in permanent shadow. Areas where radar-bright features coincide with a PSR appear in brick orange. The Sapkota and Burke craters are labeled in green. The map is limited to latitudes >75°N. Over the six-day observing run, the radar beam is on average illuminating the area from the direction of 321°W.

3.1. Scattering Properties of Radar-bright Features and Background Terrain

To investigate radar scattering, we first produced a radar incidence angle map independent of the radar observations using high-resolution (500 m pixel^{-1}) MESSENGER topography data based on MLA altimetric profiles (Zuber et al. 2012). Following a methodology similar to Mazarico et al. (2011) and Hamill et al. (2020), illumination from Earth as a light source was simulated for each observation day. The obtained mask of visibility was then applied to a map of the computed incidence angle of Earth's direction on the rough surface (i.e., the normal vectors defined by the topographic model). We produced a single incidence angle map by averaging over the observing campaign. In the final product, areas that were never sampled by the radar during the six-day campaign appear in the radar shadow. Finally, the maps were downsampled to have the same resolution as the radar backscatter maps. The final, campaign averaged radar incidence angle map is shown in Figure 4. The maximum incidence angle is set to 85° because for higher incidence angles $1/\beta$ in basalt-like rock is less than that in the S-band wavelength. The minimum incidence angle in the study area is ∼40°, which is near the identified global transition to diffuse scattering for OC in Figure 1.

The SC and OC radar backscatter coefficient maps were coregistered with the incidence angle map. In Figure 5, we show σ^0 and the respective incidence angle for the identified polar-bright features and background terrain. We also show the circular polarization ratio (i.e., $\mu_c = \sigma_{SC}/\sigma_{OC}$) as a function of incidence angle. The SC and OC radar backscatter coefficients of the DBSCAN-identified polar-bright features is readily distinguishable from the background with little to no overlap (Figures 5(a) and (b)). As such, the small, seemingly radar-bright features, such as the diffuse patch, that were not automatically detected by the DBSCAN procedure are likely better characterized by the scattering behavior of the background terrain. This could suggest that such features may have little to no ice. Furthermore, the background terrain has a flat response to incidence angle, while the polar features have a seemingly negative linear relationship with incidence angle. Indeed, surface roughness should lead to a rather flat response in SC and OC backscatter for $30° \lesssim \phi \lesssim 70°$ (Fa et al. 2011; Thompson et al. 2011). As such, the observed decrease in SC and OC radar backscatter as a function of incidence angle for the radar-bright features is likely not due to surface roughness alone.

Additionally, we find that there is significant overlap between the background and bright feature circular polarization ratio (Figure 5(c)). In fact, high μ_c can occur at high incidence
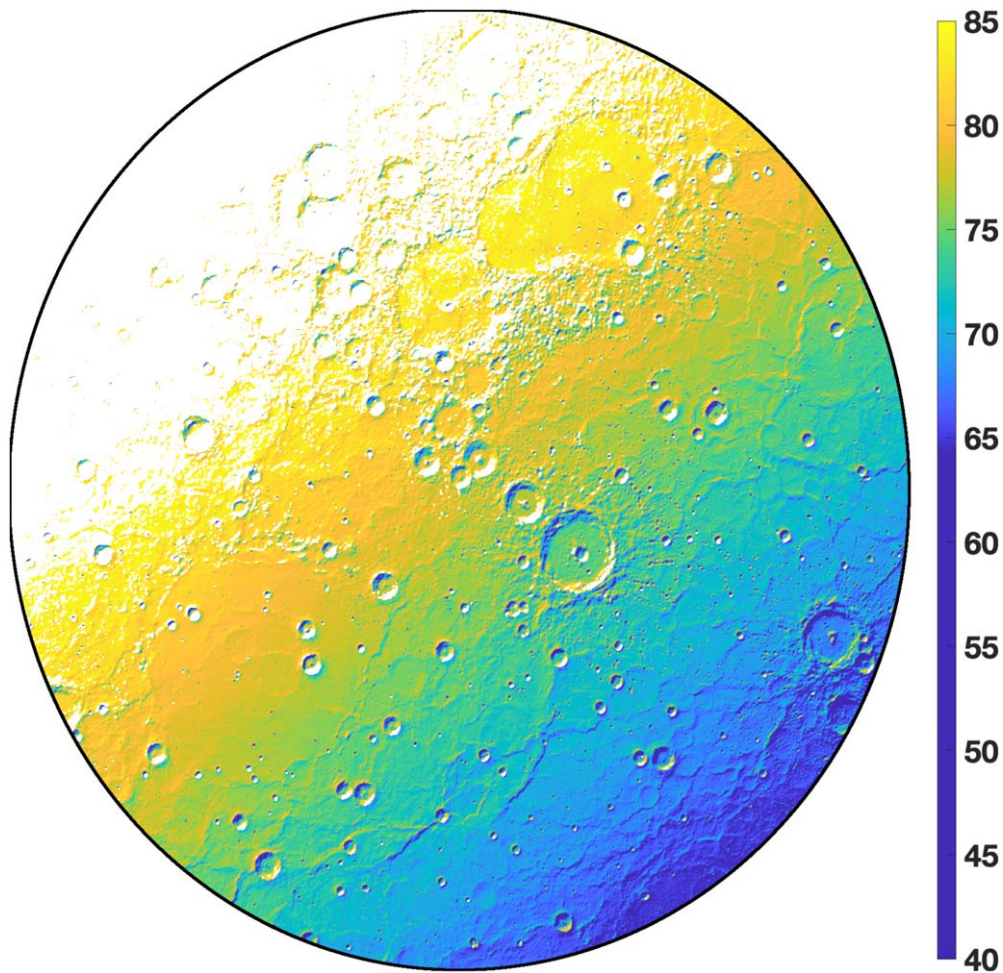
Figure 4. Simulated campaign average incidence angle map for our radar observations. In color, the incidence angle increases from 40° to 85° with a stretched color map so as to improve visualization of the incidence angle gradient across the scene. Areas that were never sampled by radar during our observing campaign or were at incidence angles >85° appear in white. The map is limited to latitudes >75°N.

angles even for nonicy surfaces (Fa et al. 2011; Thompson et al. 2011). As such, μ_c may not be a robust diagnostic tool to identify volatile deposits. Indeed, Virkki & Bhiravarasu (2019) suggest a comparison of σ_{OC}^0 and σ_{SC}^0 (Figure 5(d)) as a more appropriate diagnostic tool. In Figure 5(d), the background terrain and bright features are clearly distinguishable as two different populations. As observed for the Moon (Virkki & Bhiravarasu 2019), there is a positive linear relationship between σ_{OC}^0 and σ_{SC}^0. The background terrain follows a more cone-like distribution, while the bright features are more dispersed. A least-squares fit to each population results in a y-intercept for the background and polar features of 0.02 and 0.08, respectively. Following the work of Virkki & Bhiravarasu (2019), this may suggest that the background terrain has a lower effective dielectric permittivity than the polar features. Furthermore, the least-squares fit slope of the radar-bright features is 0.14 while that of the background terrain is 0.17, suggesting the bright features are generally enhanced in SC backscatter, as expected from water ice.

3.2. Constraints on Ice Purity

Previously, Butler et al. (1993) investigated the scattering properties of the radar-bright features at Mercury's north pole

to constrain their purity. By comparing the reflectivity of the Mercurian polar-bright features to that of the Martian residual south polar ice cap along with a Monte Carlo model of radar attenuation, Butler et al. (1993) found that the radar reflector within PSRs is likely nearly pure water ice with at most a 5% contribution from an absorbing material. Comparison between MESSENGER MDIS images and high-resolution models of the thermal environments within some craters indicates that ice within some PSRs is likely buried under a low-reflectance, potentially organic-rich, material (Neumann et al. 2013; Chabot et al. 2014, 2016, 2018a; Hamill et al. 2020), on the order of 10–20 cm thick (Lawrence et al. 2013). This could suggest that the PSR ice deposits have sufficient impurities to produce a sublimation lag, which could imply a higher expected impurity fraction within the ice deposits than previously inferred.

Here, in order to study the bulk properties of the PSR radar reflector, we used radar-scattering models of σ_{OC}^0 to constrain the dielectric permittivity and wavelength-scale regolith physical properties. Various radar-scattering models have been developed to describe the behavior of received echoes as a function of incidence angle (e.g., Hagfors 1964; Mitchell et al. 1996). In investigating the background terrain, we applied the Hagfors scattering function, which was developed originally to model the lunar radar echo and describes the change in σ_{OC}^0 as a
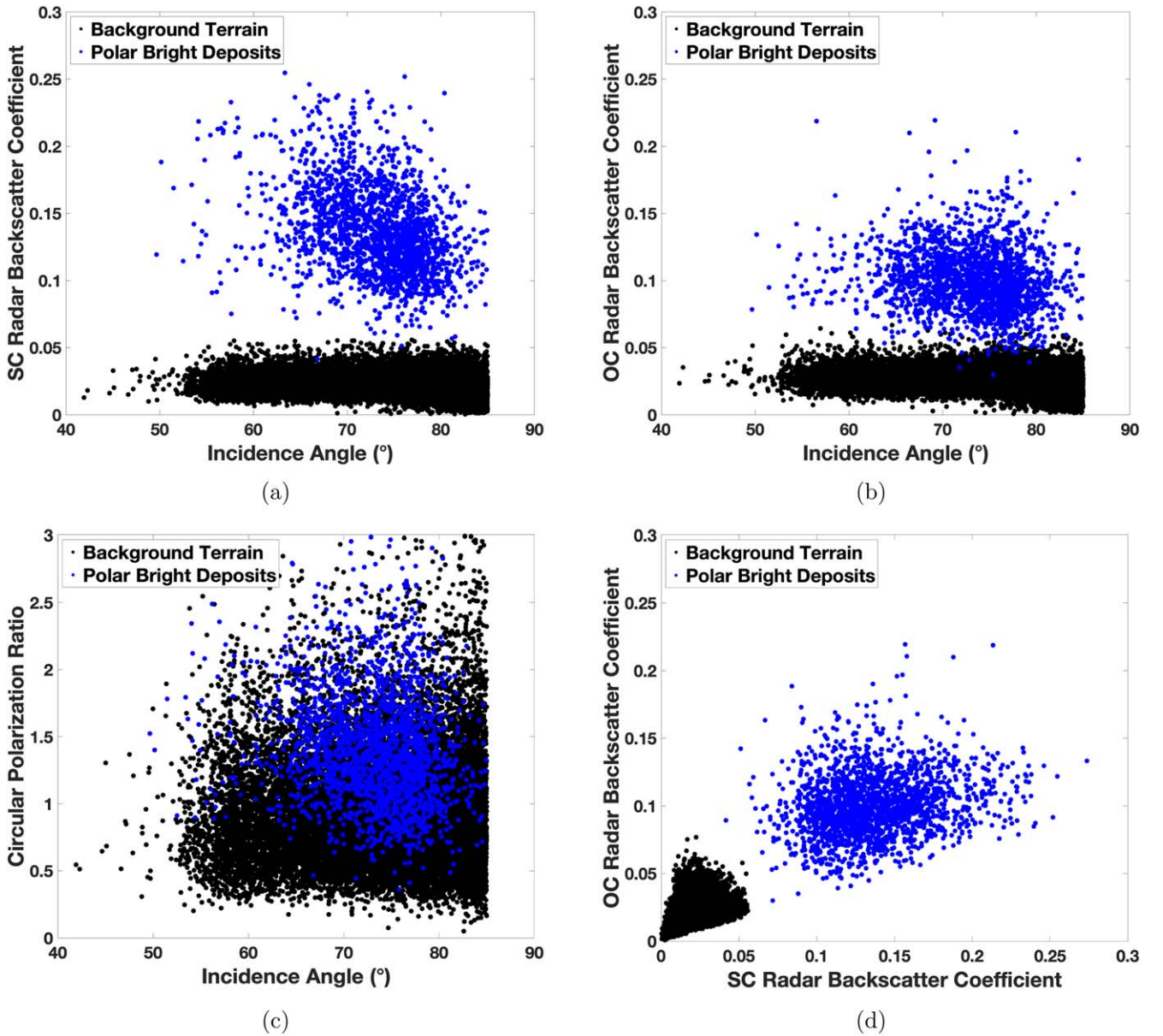
Figure 5. Measured radar scattering of the background terrain (black) and radar-bright features (blue) as a function of incidence angle. In (a) and (b), we plot the radar backscatter coefficients in SC and OC, and in (c) the circular polarization ratio. In (d), we show the relationship between the SC and OC radar backscatter coefficients of the northern polar terrain (σ_{SC}^0 and σ_{OC}^0).

function of incidence angle as

$$\sigma_{OC}^0 = \frac{R_0 C}{2(\cos^4 \phi + C \sin^2 \phi)^{3/2}}, \qquad (7)$$

where $C = \alpha^{-2}$, α is the rms average value of undulating surface slopes in units of radians, and R_0 is the Fresnel power reflection coefficient, which is a function of the dielectric permittivity as

$$R_0 = \left(\frac{1 - \sqrt{\epsilon_r}}{1 + \sqrt{\epsilon_r}}\right)^2. \qquad (8)$$

We calculated the reduced χ^2 (i.e., χ^2 per degree of freedom) parameter to identify the values of ϵ_r and C required to best fit the measured σ_{OC}^0 of the background terrain. The data were binned by incidence angle in steps of 2°. The average and

standard deviation of the binned radar backscatter coefficients are then compared to those of the modeled σ_{OC}^0 to calculate the test statistic for a range of ϵ_r and C. In Figure 6(a), we show the calculated reduced χ^2 over the free parameters and identify the set of ϵ_r and, for plotting purposes, α in units of degrees that result in a reduced $\chi^2 \sim 1$, which is considered the most likely combination of parameters to represent the observed scattering behavior. Although the Hagfors scattering law can produce functions where the radar backscatter coefficient at low incidence angle is lower than at high incidence angle, such solutions are considered unrealistic. Here, we only considered viable those solutions that result in a scattering law with higher σ_{OC}^0 at low incidence angles. Given Equation (7), this results in solutions where $C \geqslant 1$ or $\alpha \leqslant 57°$.

We found that for the background terrain, the best-fit realistic parameters are likely in the range of $1 \lesssim C \lesssim 2$ (i.e., between
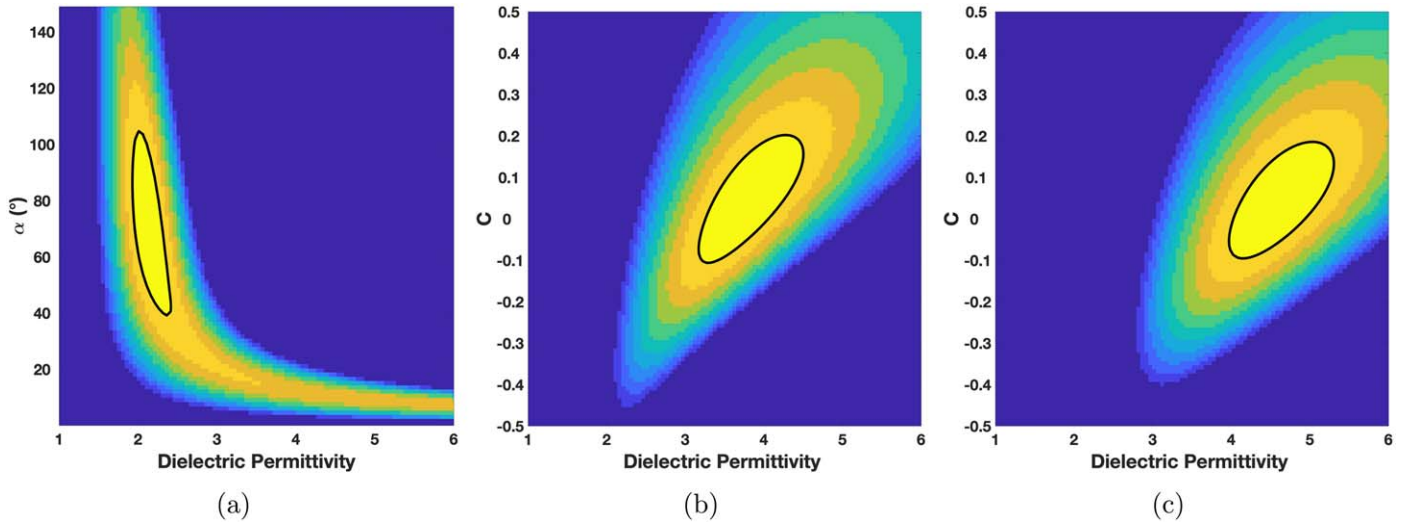
Figure 6. Calculated reduced χ^2 (i.e., χ^2 per degree of freedom) over the free parameters for the fits to (a) Equation (7) for the background terrain and Equation (10) for the radar-bright features with (b) $\mu_c > 1$ (b) and (c) $\mu_c < 1$. The color map is clipped to show the reduced χ^2 from zero to ten. The black ellipse is a contour of $\chi^2 = 1$, which is where the combination of best-fit parameters likely lie.

~40° and 57°) and $2 \lesssim \epsilon_r \lesssim 2.5$. The range of inferred dielectric values is similar to what was measured for the Moon using the Mini-RF radar instrument at the S band (Heggy et al. 2020) and agrees well with derived values from radio (not radar) observations of Mercury, which derived a hemispheric average $\epsilon_r \sim 2$ (Burns et al. 1987; Ledlow et al. 1992). This may suggest that on a global scale there is little variation in the bulk regolith properties and that it is well described by a porous lunar-like regolith. Following a time-propagation, volumetric dielectric mixing model (Knoll 1996), which is a specific case of the Lichtenecker–Rother equation (Lichtenecker & Rother 1931), and assuming the primary constituent of Mercury's regolith is basalt rock, the porosity of the terrain can be approximated as

$$\vartheta \approx \frac{\sqrt{\epsilon_{\text{eff}}} - \sqrt{\epsilon_B}}{\sqrt{\epsilon_V} - \sqrt{\epsilon_B}}, \quad (9)$$

where ϵ_{eff} is the measured effective dielectric permittivity, and $\epsilon_B \sim 8$ and $\epsilon_V = 1$ are the dielectric permittivities of bulk basalt rock and vacuum, respectively. As such, the bulk porosity of the background terrain as constrained by S-band radar is $0.60 \lesssim \vartheta \lesssim 0.77$, which agrees well with the porosity derived from whole-disk spectrophotometric measurements (Domingue et al. 2010). Given agreement with other measurements, these results imply that the Hagfors scattering model, originally developed for the Moon, is well suited to describe the general scattering behavior of the Mercurian regolith, even at high incidence angles.

Although the Hagfors scattering model best describes the general, quasi-specular scattering function of lunar-like planetary surfaces, it would not describe well the highly diffuse nature of scattering within ice. To resolve the properties of the radar-bright deposits, we employed a cosine scattering function of the form

$$\sigma^0_{\text{OC}} = R_0 (C + 1) \cos^{2C} \phi. \quad (10)$$

Here, C does not necessarily directly correlate with rms slopes. Fundamentally, C is the shape parameter of the σ^0_{OC} function and has known limitations based on previous derivations

(Sultan-Salem & Tyler 2006). Its physical meaning, particularly for scattering within ice, is a topic of continued research, including much-needed experimental validation. As seen in Figure 5, some radar-bright features have $\mu_c < 1$, which, following CBOE, would not be associated with coherent scattering within ice. As such, we divided the data and fit for those values related to a DBSCAN-identified radar-bright feature with $\mu_c > 1$, likely related to CBOE, and $\mu_c < 1$, likely little to no ice. We followed the same methods as for the background terrain to find the reduced χ^2 to identify the best-fit parameters.

For values with $\mu_c > 1$ (Figure 6(b)), we found that the best-fit parameters are likely in the range of $-0.10 \lesssim C \lesssim 0.20$ and $3.3 \lesssim \epsilon_r \lesssim 4.5$. Thus, the dielectric permittivity of the radar-bright features is higher than that of the background terrain as inferred from Figure 5(d). Our derived dielectric permittivity for the polar deposits is somewhat higher than the inferred dielectric permittivity of the Martian polar deposits, $\epsilon_r \sim 3.1$ (Grima et al. 2009) and significantly higher than that of the nucleus of comet 67P/CG, $\epsilon_r \sim 1.3$ (Hérique et al. 2016). The dielectric permittivity of water ice is $\epsilon_r = 3.2$ (Matzler & Wegmuller 1987), decreasing slightly to 3 at temperatures below 200 K (Gough 1972), and is not significantly sensitive to the ice phase, e.g., hexagonal versus amorphous (Gough 1972; Andersson 2008). As such, the inferred high dielectric permittivity may be caused by the addition of a high dielectric impurity within the ice, which is expected given the dark, sublimation lag identified within some PSRs. Indeed, modeling work by Fa et al. (2011) of radar scattering from potential ice deposits within lunar PSRs finds that for $\epsilon_r > 3$, the likely structure is pure ice with silicate grain inclusions while for $\epsilon_r < 3$ it is porous ice mixed with silicates.

For values with $\mu_c < 1$ (Figure 6(c)), we found that the best-fit parameters are likely in the range of $-0.10 \lesssim C \lesssim 0.18$ and $4.0 \lesssim \epsilon_r \lesssim 5.3$. The best-fit C parameter is similar for radar-bright features regardless of μ_c. On the other hand, the inferred dielectric permittivity of the low-circular-polarization ratio values is generally higher than that of the high-μ_c values. There may therefore be differences in ice purity across the radar-bright features.

As such, we investigated the ice purity of features with high and low circular polarization ratios. Considering water ice with an absorbing impurity modeled as spherical inclusions of basalt within solid ice, the effective bulk dielectric permittivity of the PSRs can be modeled following the Maxwell–Garnett formula (Sihvola & Sharma 1999) as

$$\epsilon_{\text{eff}} = \epsilon_{\text{ice}} + 3f\epsilon_{\text{ice}}\left(\frac{\epsilon_B - \epsilon_{\text{ice}}}{\epsilon_B + 2\epsilon_{\text{ice}} - f(\epsilon_B - \epsilon_{\text{ice}})}\right), \qquad (11)$$

where f is the volume fraction of impurity, $3 \leqslant \epsilon_{\text{ice}} \leqslant 3.2$ and $6 \leqslant \epsilon_B \leqslant 8$ are the dielectric permittivities of ice and basalt, respectively. Given the inferred dielectric permittivity for the radar-bright features with $\mu_c > 1$ and $\mu_c < 1$ and the range of possible ϵ_{ice} and ϵ_B, we calculated the volume fraction of impurity in the ice. For $\mu_c > 1$, we considered the lower and upper bound values from the χ^2 fits of $\epsilon_r = 3.3$ and $\epsilon_r = 4.5$. We found that $0.03 \leqslant f \leqslant 0.13$ for $\epsilon_r = 3.3$ and $0.36 \leqslant f \leqslant 0.57$ for $\epsilon_r = 4.5$. Similarly, for $\mu_c < 1$, we found that $0.23 \leqslant f \leqslant 0.40$ for $\epsilon_r = 4.0$ and $0.54 \leqslant f \leqslant 0.81$ for $\epsilon_r = 5.3$. Indeed, experimental work by Heggy et al. (2007) showed that $\epsilon_r \sim 3$ results in $0.05 \leqslant f \leqslant 0.2$ and $\epsilon_r \sim 5$ results in $f > 0.8$ at the S band and a temperature of $180\,\text{K}$ for ice with a density of $0.8\,\text{g cm}^{-3}$ (Thompson et al. 2011). Thus, the location of $\mu_c > 1$ is likely associated with nearly pure water ice while $\mu_c < 1$ is likely associated with water-ice-rich regolith. Additionally, at the location of $\mu_c > 1$, the previous findings of Butler et al. (1993), which suggested the ice was nearly pure water ice with an impurity volume fraction of no more than 5%, continue to be a possible solution using our different approach, that of modeling radar scattering.

Considering those solutions to the scattering model that permit a high impurity volume fraction in the ice for deposits with $\mu_c > 1$, we note that such levels of impurity would likely impede the coherent backscatter effect. Due to the large ϵ_i for basalt rocks, such inclusions in the ice act as strong absorbers, significantly reducing backscatter efficiency. A potential analog to consider is Ganymede where coherent backscattering may result in high OC and SC radar albedos (Black et al. 2001). Spectral observations across multiple frequencies of Ganymede's surface suggest it may have a nonicy component of at most $\sim20\%$ (Spencer 1987; de Kleer et al. 2021). This may imply that the high dielectric permittivity values permitted by the scattering model for $\mu_c > 1$ may not be realistic given the high radar backscatter coefficients in both polarizations measured at the high incidence angles over Mercury's north pole. Alternatively, the inferred high ϵ_r values may be indicative of a high-dielectric and modest-loss material such as planetary-relevant polymers (Thompson & Squyres 1990) and ices, like water-ammonia ices (Lorenz 1998), with $\epsilon_r \sim 5$. For example, Hamill et al. (2020) found that the spatial boundaries of the MLA dark material correlated closely with the thermal stability boundary for coronene ($C_{24}H_{12}$), which for frequencies $<1\,\text{MHz}$ has been shown to have a maximum dielectric permittivity of $\epsilon_r \sim 6.5$ (Akin et al. 2021).

It is important to note that the constraints developed here are sensitive to the choice of radar-scattering model, as well as the permittivity mixing model. Investigating the scattering behavior of Mercury's radar-bright features requires scattering models that account for coherent backscattering in a robust manner, as well as the expected complex nature of the deposits (e.g., ice below a lossy, potentially organic, overburden). Furthermore, experimental studies of radar backscattering as a function of incidence angle from ice and ice buried beneath a lossy mantling are needed to help constrain modeling approaches.

3.3. Local-scale Variations

To contextualize the inferred compositional differences across the radar-bright features, they were further analyzed for local-scale variations. Comparing pixel-by-pixel σ^0 variations, though, is not robust in high-resolution radar images because the true uncertainty of each value is not well constrained because the noise statistics are non-Gaussian (e.g., Nolan et al. 2013). This typically leads one to coarsen the image resolution in order to increase the overall S/N and improve confidence in pixel-by-pixel comparison. Here, in order to preserve spatial resolution while robustly identifying differences in backscatter, we applied a k-means clustering algorithm over the σ^0_{SC} of only the bright features. We focus on SC because it will be the most sensitive to multiple scattering events within the ice.

The k-means clustering method is an iterative algorithm that partitions data into groups by minimizing within-cluster variances (Lloyd 1982). The algorithm is initiated by randomly choosing the k number of cluster centers then calculating the point-to-cluster distances and assigning data closest to the cluster center to those groups. The average of the data within the group is then used as the next cluster center. Here, we iterate this process until either cluster assignments do not change or a maximum of 1000 iterations has occurred. Furthermore, the process is replicated 10 times to find the optimum solution. Typically, k-means is supervised as it requires a predetermined number of clusters; however, the technique can be made unsupervised by optimizing the so-called CH index (Calinski & Harabasz 1974), which identifies the best number of groups by maximizing the ratio of the sum of between-cluster and intercluster dispersion, where a system without an optimum CH index may not be clusterable. Using k-means, we find the best cluster centers and corresponding CH parameter for $2 \leqslant k \leqslant 20$ in increments of 1. The optimum number of classes is then identified by finding the k associated with the maximum CH index. A data set that produces a smooth (i.e., flat, increasing, or decreasing) CH index as a function of k is considered not clusterable. Additionally, we further restricted the number of classes by ensuring that the range of values represented in a group was no finer than the 20% calibration uncertainty. This technique has been previously applied to planetary data sets and has proven robust in identifying differences in, e.g., ice phase and crystallinity (Dalle Ore et al. 2015, 2021). Clusters are then represented by their mean SC backscatter ($\overline{\sigma^0_{\text{SC}}}$) and standard deviation such that different clusters represent significant differences.

In Figure 7, we show the $\overline{\sigma^0_{\text{SC}}}$ cluster locations overlaid on a MESSENGER MDIS image of the north polar terrain. Significant local-scale variations in SC radar backscatter of the north polar deposits are distinguishable in both the large and small craters. While the radar-bright feature within the crater floor of Prokofiev and other nearby small craters has a mottled appearance, Chesterton, Tolkien, and Tryggvadóttir, as well as the central peak of the Prokofiev craters have a clear pattern. The centers of these, and several surrounding craters,
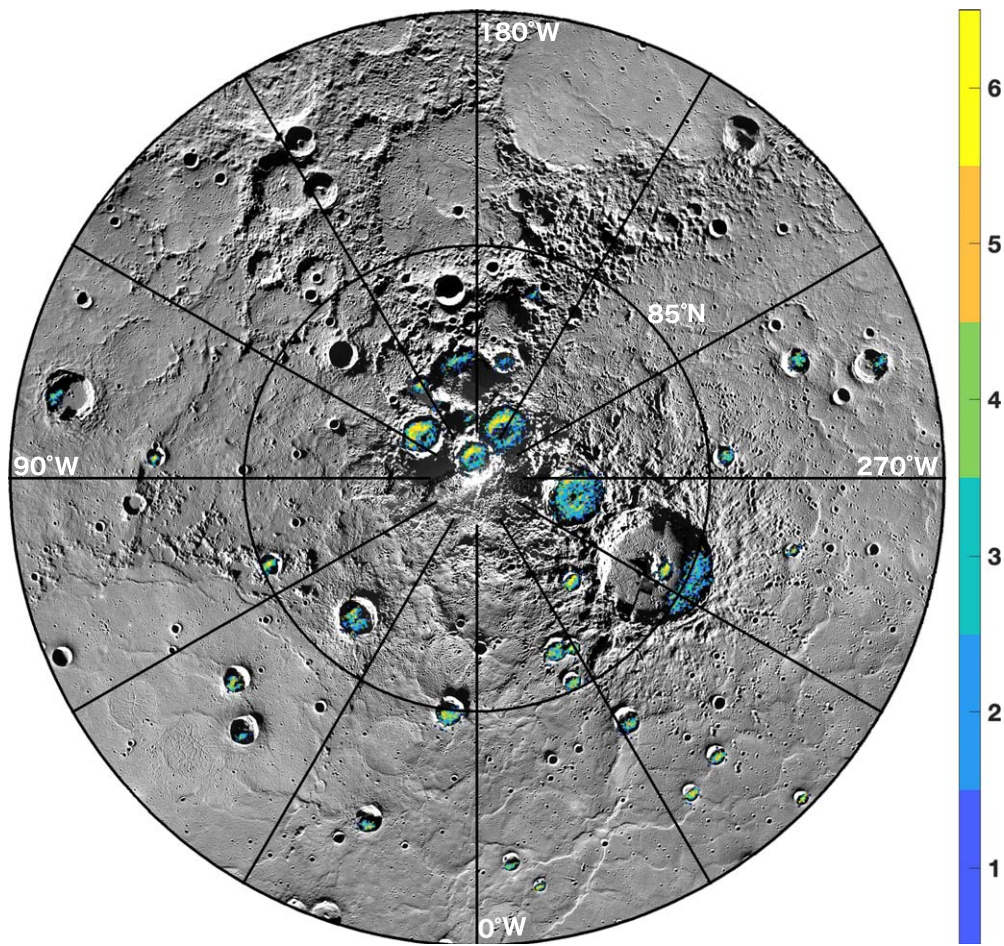
Figure 7. Overlay of the k-means classes of SC radar backscatter onto a MESSENGER MDIS image of the northern polar terrain. The classes are in color from blue (class 1) to yellow (class 6) as low to high SC radar backscatter. In Table 2, we show the class mapping to the mean and standard deviation of the SC radar backscatter coefficients within each class. The map is limited to latitudes >80°N.

partition into the highest k-means classes, grading to lower classes with distance from their centers.

One possible explanation for the observed gradation is ice-purity differences, as discussed earlier. As summarized in Table 3, the circular polarization ratio increases with k-means class and is on average <1 for the lowest classes. We find that more than 96% of the data within k-means classes >4 have $\mu_c > 1$, sharply decreasing to only ∼30% for class 1 values. As such, on average, the gradation observed in Chesterton, Tolkien, Tryggvadóttir and other small craters is both in terms of SC and in circular polarization ratio. As noted before, $\mu_c < 1$ values would suggest that CBOE is not occurring and our modeling showed that such values correspond to an impurity volume fraction of $f > 0.23$. Considering that the $\mu_c < 1$ values surround the highest k-means classes, which our scattering model suggested were composed of nearly pure ice, then the gradation observed in some craters is a gradient in ice purity. Indeed, as can be seen in Table 2, this gradient does not correspond to significant changes in the radar incidence angle and so is not likely due to radar backscatter enhancement due to topography.

The identified gradient in ice purity within some deposits may be due to impact-induced lateral mixing. Lateral transport of material has been shown to occur on the Moon due to impact gardening over some 4–5 km (Li & Mustard 2000). In fact, Chabot et al. (2014) suggested that lateral transport of water ice

Table 3
Mean Values and Standard Deviation for the SC Radar Backscatter k-means Analysis Shown in Figure 7

Class	$\overline{\sigma^0_{SC}}$	$\overline{\sigma^0_{OC}}$	$\overline{\mu_c}$	$\overline{\phi}(°)$
1	0.08 ± 0.01	0.10 ± 0.03	0.93 ± 0.33	75 ± 5
2	0.10 ± 0.01	0.10 ± 0.02	1.16 ± 0.29	75 ± 4
3	0.12 ± 0.01	0.10 ± 0.02	1.30 ± 0.33	74 ± 5
4	0.14 ± 0.01	0.10 ± 0.02	1.45 ± 0.33	73 ± 5
5	0.16 ± 0.01	0.10 ± 0.02	1.62 ± 0.34	71 ± 5
6	0.20 ± 0.02	0.11 ± 0.02	1.89 ± 0.37	69 ± 6

may occur within the Prokofiev crater. In their work, they found that the boundaries of the radar-bright features and the optically bright features observed in MESSENGER MLA and WAC images were offset by a few kilometers (Chabot et al. 2014), which could be related to lateral mixing. Alternatively, the gradation may be the result of the thermal environment. Indeed, thermal models suggest that areas with surface or near-surface ice are surrounded by a zone of subsurface ice (Paige et al. 2013). The deeper, subsurface ice would result in reduced radar backscatter due to scattering from the regolith mantling.

Furthermore, we found that there is little to no difference in the average OC radar backscatter associated with the highest $\overline{\sigma^0_{SC}}$ values. While the top k-means class is associated with a
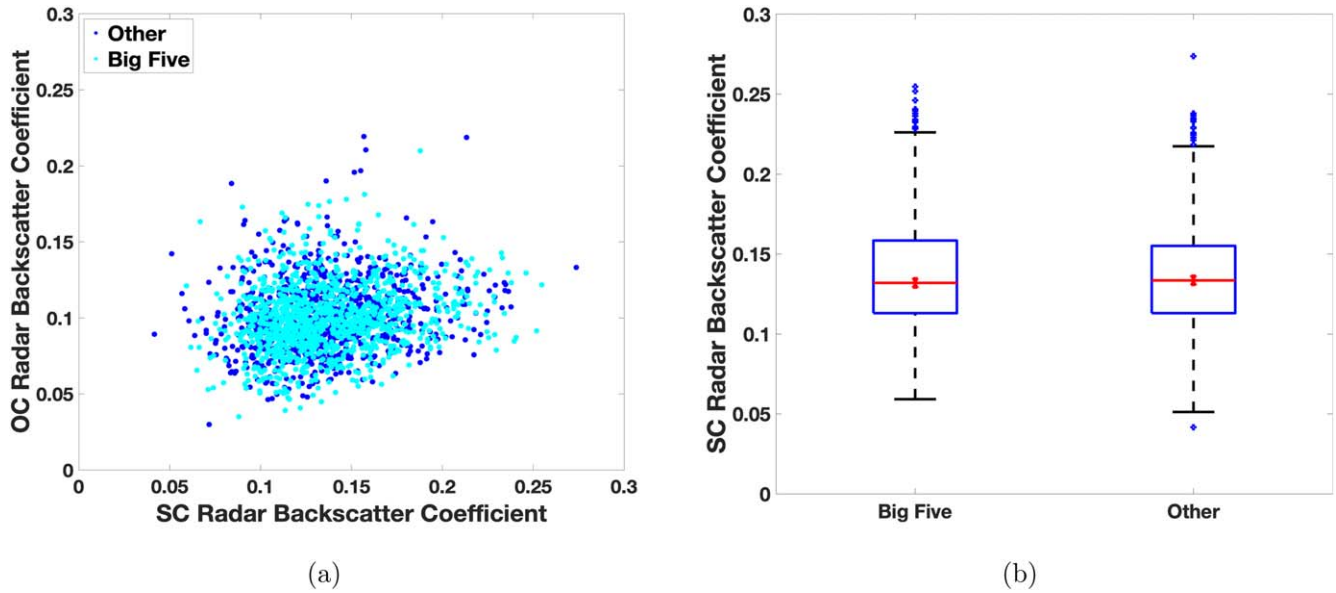
(a) (b)

Figure 8. Scattering properties of the radar-bright features associated with the big five craters, Prokofiev, Kandinsky, Tolkien, Tryggvadóttir, and Chesterton, which may have surficial ice deposits, compared to all other radar-bright features, which likely represent ice deposits buried underneath a thin mantling. In (a), we show the SC and OC radar backscatter coefficient for the big five craters (cyan) and all other radar-bright features (blue). In (b), we show a box plot of the SC radar backscatter coefficient of the big five craters and all other radar-bright features. The red line denotes the median of the data set, the blue box encapsulates the interquartile range, the whiskers are the black dashed lines and represent a distance of 1.5 times above/below the interquartile range, and the blue crosses denote outlying data.

corresponding average σ_{OC}^0 of 0.11 ± 0.02, while the lowest class corresponds to an average σ_{OC}^0 of 0.10 ± 0.03. The significant difference in $\overline{\sigma_{SC}^0}$ with no corresponding significant change in OC backscatter could indicate further differences in ice purity across the highest k-means classes. These differences could be caused by increasing basalt inclusions within the ice. Such detailed differences, though, are too fine to capture with dielectric mixing models. The k-means study of radar backscatter could thus suggest that the highest cluster of σ_{SC}^0 could indicate the purest ice deposits. Assuming this is the case, we can estimate the thickness of the ice deposits over these regions. Typically (i.e., the interquartile range), the radar incidence angle of the highest k-means class is within 66° and 73°. Assuming pure water ice, the radar beam may be sampling a depth normal to the surface of 10–15 m over these deposits. This depth is consistent with estimates for the upper limit of the ice thickness of 15 m based on MLA-measured topography changes over the location of radar-bright features (Susorney et al. 2019).

The top k-means of σ_{SC}^0, though, occurs in clusters within both large and small craters. In fact, there is no readily identifiable association between the top k-means classes and crater size or location. This would then suggest that the purest ice deposits are not only associated with the largest craters, where ice is suggested to be the most stable. Thermal modeling suggests that the conditions within Prokofiev, Kandinsky, Tolkien, Tryggvadóttir, and Chesterton would permit surface ice to be stable over geologic time (Paige et al. 2013; Chabot et al. 2018a). Indeed, Chabot et al. (2014) and Neumann et al. (2013) identified higher-reflectance regions within the PSR of Prokofiev in both MESSENGER WAC broadband images and MLA reflectance data, indicative of a surficial ice deposit. However, only the PSR near the central peak of the Prokofiev crater displays the gradational pattern in SC backscatter as seen

in Tolkien, Chesterton, and Tryggvadottír; its large PSR displays a rather mottled distribution in SC radar backscatter.

While the Prokofiev, Kandinsky, Tolkien, Tryggvadóttir, and Chesterton craters may have surficial ice deposits, as seen in Figure 7, not all of these craters are associated with the highest radar backscatter. Furthermore, as can be seen in Figure 8(a), the SC and OC radar backscatter of these big five craters and the other radar-bright features is largely indistinguishable. Indeed, the least-squares fit slopes for the big five craters and other radar-bright features, respectively, are 0.15 and 0.13, which suggest these features, overall, have similar SC enhancements, and y-intercepts are both 0.08, which suggest these features generally have a similar dielectric permittivity. Additionally, in Figure 8(b), we also show a box plot displaying the distribution of σ_{SC}^0 within the big five craters and the other radar-bright features. As can be seen, the interquartile ranges overlap as do the medians and so there is no evidence to suggest that the two populations of σ_{SC}^0 are different.

Deutsch et al. (2017) identified enhanced MLA reflectance indicative of exposed ice in smaller craters with diameters less than 5 km and microcold traps in the intercrater terrain. Their work would suggest that surface ice deposits may exist outside of the big five polar craters. This could explain why there is no readily identifiable difference in the radar-scattering properties of these and other craters. Alternatively, surface ice may be thin enough that it does not result in differences in radar backscatter. The exposed ice could be thick enough to result in a 1064 nm reflectance difference in MLA data while thin enough to result in a negligible effect on S-band radar observations. This could restrict the surficial ice deposits to a few centimeters. Such thin deposits could be the result of impact gardening within the PSRs. Additionally, the MLA and MDIS data simply indicate a higher reflectance value than the surrounding terrain (Neumann et al. 2013; Chabot et al. 2014, 2016, 2018a). These differences have not been used to constrain the purity of the surface ice.

The higher-reflectance surface observed in MLA and MDIS observations could be a mixture of ice and other materials. This "dirty" surface ice may explain the mottled appearance of the deposit within the floor of Prokofiev.

4. Conclusions

Here we reported on Arecibo *S*-band (12.6 cm, 2380 MHz) radar observations of Mercury during the 2019 inferior conjunction, the first taken since the end of the MESSENGER mission. Data products produced from this observing campaign were polar stereographic maps of radar backscatter in the SC and OC polarization as transmitted. MESSENGER-derived data products and results were used to enhance radar-based characterization of the north polar water ice deposits within the PSRs. We also employed two machine-learning algorithms, DBSCAN and *k*-means clustering, to automate radar-bright feature identification and analysis of local-scale variations. Specifically, we investigated intercrater differences.

MESSENGER-based, high-resolution topography was used to compute the radar incidence angle over the poles during each of the observing days. Coregistering the incidence angle with the radar backscatter maps allowed us to study the radar-scattering properties of the bright features and the background terrain. We found that the background terrain is well characterized by the Hagfors scattering model (Hagfors 1964), originally developed for the Moon. The inferred dielectric permittivity of the background terrain is $2 \lesssim \epsilon_r \lesssim 2.5$, which agrees well with values derived for the Moon (Heggy et al. 2020) and previous radio (not radar) whole-disk observations of Mercury (Burns et al. 1987; Ledlow et al. 1992). Assuming basalt rock, the dielectric permittivity of the background terrain would suggest a regolith porosity of $0.60 \lesssim \vartheta \lesssim 0.77$, which agrees well with the porosity derived from whole-disk spectrophotometric measurements (Domingue et al. 2010).

The Hagfors scattering model, though, would not adequately describe the expected highly diffuse nature of the scattering within the ice deposits. Using a cosine scattering model, we investigated the characteristic of the radar-bright features. Given that the high radar backscatter is likely due to water ice through the CBOE, we partitioned the radar backscatter of the bright features by circular polarization ratio. We found that the bright features with $\mu_c > 1$ are well characterized by a dielectric permittivity of $3.3 \lesssim \epsilon_r \lesssim 4.5$, while locations with $\mu_c < 1$ are well characterized by the dielectric permittivity of $4.0 \lesssim \epsilon_r \lesssim 5.3$. We note, though, that these inferred dielectric permittivities are model dependent and further work is needed to resolve radar scattering by CBOE as a function of incidence angles.

Modeling the inferred dielectric permittivities of the radar-bright features as a mixture of ice and basalt, we found that for locations with $\mu_c > 1$, the volume fraction of the basalt impurity is likely $\gtrsim 3\%$ while for $\mu_c < 1$ it is $\gtrsim 20\%$. Additionally, we found that typically the locations of the highest SC radar backscatter coincide with $\mu_c > 1$ and are surrounded by lower backscatter, which coincides with $\mu_c < 1$, in a gradational pattern. This pattern may suggest that the purest ice deposits in the north pole are surrounded by water-ice-rich regolith. This could be a consequence of processes such as lateral mixing induced by impact gardening (Li & Mustard 2000; Chabot et al. 2014) or the thermal environment of the crater (Paige et al. 2013). These observations may provide improved constraints on the formation of the polar ice deposits and the timing of their deposition. For example, Crider et al. (2006) used the ice-purity constraints by Butler et al. (1993) along with constraints on Mercury's weathering rate and impact history to suggest that the ice deposits may be due to a cometary impact that occurred some 50 Myr ago. However, here we show that not all of the ice deposits may represent pure ice, potentially changing the timing of the cometary impact. In fact, cometary impacts have been shown to be the likely source of lunar water at the near surface (Mandt et al. 2022) and so the state of the Mercurian deposits may help shed light on the timing of the impact. Additionally, we found that the observed gradational pattern in SC radar backscatter occurs in both large and small craters. This would suggest that the purest ice deposits are not only associated with the largest craters where ice is thought to be the most stable.

MESSENGER data suggest that the "big five" craters—Prokofiev, Kandinsky, Tolkien, Tryggvadóttir, and Chesterton—have surficial ice deposits (Neumann et al. 2013; Chabot et al. 2014, 2016, 2018a; Deutsch et al. 2017). However, we compared their scattering properties to those of the other radar-bright features and found no significant difference. The lack of a distinguishable difference in radar scattering between the big five and other craters with radar-bright features could suggest exposed water ice may exist outside of the largest polar craters. However, thermal models do not support stable surface ice within many radar-bright features. Furthermore, MESSENGER reflectance results from both MLA and MDIS show extensive low-reflectance surfaces that are inconsistent with the presence of surface water ice within many deposits. Deutsch et al. (2017), though, identified enhanced reflectance in MLA data within some small craters, of diameter less than 5 km, and microcold traps in intercrater terrain. Alternatively, surface ice may be less than a radar-wavelength thick resulting in little to no impact on radar backscatter while producing an MLA bright feature. Additionally, MESSENGER data simply indicate a higher reflectance value than the surrounding terrain, which could be a mixture of ice and other materials. Such "dirty" ice may explain those craters with a mottled pattern in their radar backscatter, such as seen on the floor of the Prokofiev crater.

Our Arecibo *S*-band radar observations paired with MESSENGER data showed that some radar-bright features within Mercurian PSRs have a gradational pattern in SC backscatter and μ_c that is likely associated with a gradient in ice purity. At the same time, there are several new outstanding questions revealed by our analysis:

1. How are the intercrater differences in ice abundance produced?

   Here we identified two general patterns in the PSR deposits. Some craters may host nearly pure water ice surrounded by decreasing ice purity while others host less pure ice with no clear spatial pattern in the deposit. Although these patterns may be produced by the crater's thermal environment, they show no clear association with crater size. Even if impact-induced lateral mixing may explain the gradational pattern within some craters, it does not readily explain the more mottled, less pure water ice deposits. Understanding these differences requires further studies of individual craters and their environmental context, including radar incidence angle. Additional radar observations under different subradar longitudes would also provide more sampling of the

deposit's scattering behavior, improving dielectric mixing modeling.

2. What is the high reflectance deposit observed in Prokofiev by MESSENGER MLA and WAC?

MESSENGER MLA and WAC observations interpreted the high reflectance within Prokofiev as potentially surficial water ice (Neumann et al. 2013; Chabot et al. 2016, 2018a). In our work, though, we found no significant difference in the radar-scattering properties of craters expected to host surficial ice and other radar-bright deposits. Furthermore, the radar back-scatter from Prokofiev follows a mottled pattern. Although this could imply that the surface ice is dirty and/or thin, further detailed analysis of the deposit's reflectance and radar backscatter is needed to improve the interpretation.

3. Are high dielectric permittivity values realistic for the polar ice deposits?

Given the MESSENGER Neutron Spectrometer results (Lawrence et al. 2013) and thermal modeling (Paige et al. 2013), we concentrated on interpreting the derived dielectric permittivity values as radar scattering from ice with basalt-like inclusions. Dielectric mixing modeling suggests that high dielectric values are the result of high concentrations of basalt inclusions. Such impurity volume fractions would significantly reduce backscatter efficiency; therefore, it would not lead to the observed radar-bright features. Alternatively, the inferred high dielectric values may be due to water ice with planetary-relevant polymers or maybe water-ammonia ices (Thompson & Squyres 1990; Lorenz 1998). Indeed, Hamill et al. (2020) suggest that the thin mantling over some ice deposits may be coronene, which at frequencies <1 MHz has a dielectric permittivity of $\epsilon_r \sim 6.5$ (Akin et al. 2021). Experimental studies of the dielectric properties of planetary-relevant ices, ice mixtures, and polymers at the S band are needed to better assess the likelihood of these models.

4. What is the physical meaning of the shape parameter, C, in the modeling of radar scattering from water ice?

Typically, the shape parameter is considered to be related to the rms average value of undulating surface slopes (Sultan-Salem & Tyler 2006); however, this relationship may not hold for scattering resulting from CBOE. Here, possible solutions to the cosine scattering law we employed included $C < 0$, which would be nonphysical if the shape parameter indeed was related to surface slopes. Further modeling, as well as experimental constraints, is needed to understand the scattering behavior of radar from ice as a function of incidence angle and the physical meaning of the fit parameters.

Forthcoming compositional characterization by the European Space Agency's Mercury Planetary Orbiter, part of the BepiColombo mission, which will enter Mercury orbit in 2025, will provide invaluable information to constrain the water content within the deposits, its distribution, and its potential source. Such measurements can further interpretations of ground-based radar observations, which sense to greater depths, and together help resolve some of these outstanding questions.

Beyond furthering the characterization of the north polar water ice deposits on Mercury, the work presented here can help improve the identification of subsurface ice reservoirs elsewhere, such as on the Moon. We found that the circular polarization ratio, which has often been used to identify likely locations of ice, is not a significant diagnostic tool as there was no difference between the circular polarization ratio of the bright features and that of the background terrain at the incidence angles of our observations. Our work shows that using the SC and OC radar backscatter independently can robustly identify scattering from subsurface water ice, as has been previously argued (Fa et al. 2011; Thompson et al. 2011; Virkki & Muinonen 2016; Virkki & Bhiravarasu 2019). Testing radar-scattering models against the Mercurian ice deposits may be useful for ice prospecting on the Moon.

ORCID iDs

Edgard G. Rivera-Valentín ● https://orcid.org/0000-0002-4042-003X
Heather M. Meyer ● https://orcid.org/0000-0002-6888-9868
Patrick A. Taylor ● https://orcid.org/0000-0002-2493-943X
Erwan Mazarico ● https://orcid.org/0000-0003-3456-427X
Sriram S. Bhiravarasu ● https://orcid.org/0000-0003-0019-6261
Anne K. Virkki ● https://orcid.org/0000-0002-4129-5381
Michael C. Nolan ● https://orcid.org/0000-0001-8316-0680
Nancy L. Chabot ● https://orcid.org/0000-0001-8628-3176

References

Akin, U., Yüksel, O. F., & Tuğluoğlu, N. 2021, Silicon, 1, doi:10.1007/s12633-021-01017-3
Andersson, O. 2008, JPCM, 20, 244115
Black, G. J. 2002, in ASP Conf. Proc. 278, Single-Dish Radio Astronomy: Techniques and Applications (San Francisco, CA: ASP), 271
Black, G. J., Campbell, D. B., & Nicholson, P. D. 2001, Icar, 151, 167
Burns, J. O., Gisler, G. R., Borovsky, J. E., Baker, D. N., & Zeilik, M. 1987, Natur, 329, 224

Butler, B. J., Muhleman, D. O., & Slade, M. A. 1993, JGR, 98, 15003
Calinski, T., & Harabasz, J. 1974, Communications in Statistics—Theory and Methods, 3, 1
Campbell, B. A. 2002, Radar Remote Sensing of Planetary Surfaces (Cambridge: Cambridge Univ. Press)
Campbell, B. A., Campbell, D. B., Margot, J. L., et al. 2007, ITGRS, 45, 4032
Campbell, D. B., Chandler, J. F., Pettengill, G. H., & Shapiro, I. I. 1977, Sci, 196, 650
Campbell, M. J., & Ulrichs, J. 1969, JGR, 74, 5867
Chabot, N. L., Ernst, C. M., Denevi, B. W., et al. 2012, GeoRL, 39, L09204
Chabot, N. L., Ernst, C. M., Denevi, B. W., et al. 2014, Geo, 42, 1051
Chabot, N. L., Ernst, C. M., Paige, D. A., et al. 2016, GeoRL, 43, 9461
Chabot, N. L., Lawrence, D. J., Neumann, G. A., Feldman, W. C., & Paige, D. A. 2018a, Mercury: The View after MESSENGER (Cambridge: Cambridge Univ. Press), 346
Chabot, N. L., Shread, E. E., & Harmon, J. K. 2018b, JGRE, 123, 666
Crider, D. H., Killen, R. M., & Vondrak, R. R. 2006, AdG, 3, 93
Dalle Ore, C. M., Cruikshank, D. P., Mastrapa, R. M. E., Lewis, E., & White, O. L. 2015, Icar, 261, 80
Dalle Ore, C. M., Long, C. J., Nichols-Fleming, F., et al. 2021, PSJ, 2, 83
de Kleer, K., Butler, B., de Pater, I., et al. 2021, PSJ, 2, 5
Deutsch, A. N., Chabot, N. L., Mazarico, E., et al. 2016, Icar, 280, 158
Deutsch, A. N., Head, J. W., Chabot, N. L., & Neumann, G. A. 2018, Icar, 305, 139
Deutsch, A. N., Head, J. W., III, & Neumann, G. A. 2019, E&PSL, 520, 26
Deutsch, A. N., Neumann, G. A., & Head, J. W. 2017, GeoRL, 44, 9233
Domingue, D. L., Vilas, F., Holsclaw, G. M., et al. 2010, Icar, 209, 101
Eke, V. R., Lawrence, D. J., & Teodoro, L. F. A. 2017, Icar, 284, 407
Ester, M., Kriegel, H.-P., Sander, J., & Xu, X. 1996, in Proc. Second Int. Conf. on Knowledge Discovery in Databases and Data Mining (Palo Alto, CA: AAAI), 226
Fa, W., Wieczorek, M. A., & Heggy, E. 2011, JGRE, 116, E03005
Gough, S. R. 1972, CaJCh, 50, 3046
Grima, C., Kofman, W., Mouginot, J., et al. 2009, GeoRL, 36, L03203
Hagfors, T. 1964, JGR, 69, 3779
Hamill, C. D., Chabot, N. L., Mazarico, E., et al. 2020, PSJ, 1, 57
Hapke, B. 1990, Icar, 88, 407
Hapke, B., & Blewett, D. 1991, Natur, 352, 46
Harcke, L. J. 2005, PhD thesis, Stanford Univ.
Harmon, J. K. 1997, AdSpR, 19, 1487
Harmon, J. K. 2002, ITGRS, 40, 1904
Harmon, J. K., & Campbell, D. B. 1988, Mercury (Tucson, AZ: Univ. Arizona Press), 101
Harmon, J. K., Perillat, P. J., & Slade, M. A. 2001, Icar, 149, 1
Harmon, J. K., & Slade, M. A. 1992, Sci, 258, 640
Harmon, J. K., Slade, M. A., & Rice, M. S. 2011, Icar, 211, 37
Harmon, J. K., Slade, M. A., Velez, R. A., Crespo, A., & Dryer, M. J. 1994, Natur, 369, 213

Heggy, E., Clifford, S. M., Younsi, A., et al. 2007, LPSC, 38, 1756
Heggy, E., Palmer, E. M., Thompson, T. W., Thomson, B. J., & Patterson, G. W. 2020, E&PSL, 541, 116274
Hérique, A., Kofman, W., Beck, P., et al. 2016, MNRAS, 462, S516
Knoll, M. D. 1996, PhD thesis, Univ. British Columbia, doi:10.14288/1.0052324
Lawrence, D. J., Feldman, W. C., Goldsten, J. O., et al. 2013, Sci, 339, 292
Ledlow, M. J., Burns, J. O., Gisler, G. R., et al. 1992, ApJ, 384, 640
Li, L., & Mustard, J. F. 2000, JGR, 105, 20431
Lichtenecker, K., & Rother, K. 1931, PhyZ, 32, 255
Lloyd, S. P. 1982, ITIT, 28, 129
Lorenz, R. D. 1998, Icar, 136, 344
Mandt, K. E., Mousis, O., Hurley, D., et al. 2022, NatCo, 13, 1
MATLAB development team 2020a, MATLAB k-means Module (MA, USA: The MathWorks, Natick), https://www.mathworks.com/help/stats/kmeans.html
MATLAB development team 2020b, MATLAB DBSCAN Module (MA, USA: The MathWorks, Natick), https://www.mathworks.com/help/stats/dbscan.html
Matzler, C., & Wegmuller, U. 1987, JPhD, 20, 1623
Mazarico, E., Neumann, G. A., Smith, D. E., Zuber, M. T., & Torrence, M. H. 2011, Icar, 211, 1066
Mitchell, D. L., Ostro, S. J., Hudson, R. S., et al. 1996, Icar, 124, 113
Neish, C. D., Blewett, D. T., Harmon, J. K., et al. 2013, JGRE, 118, 2247
Neumann, G. A., Cavanaugh, J. F., Sun, X., et al. 2013, Sci, 339, 296
Nolan, M. C., Magri, C., Howell, E. S., et al. 2013, Icar, 226, 629
Ostro, S. J. 1993, RvMP, 65, 1235
Ostro, S. J., Campbell, D. B., Simpson, R. A., et al. 1992, JGR, 97, 18227
Paige, D. A., Siegler, M. A., Harmon, J. K., et al. 2013, Sci, 339, 300
Paige, D. A., Wood, S. E., & Vasavada, A. R. 1992, Sci, 258, 643
Pettengill, G. H., & Dyce, R. B. 1965, Natur, 206, 1240
Pettengill, G. H., Zisk, S. H., & Thompson, T. W. 1974, EM&P, 10, 3
Prockter, L. M., Ernst, C. M., Denevi, B. W., et al. 2010, Sci, 329, 668
Rahmah, N., & Sukaesih Sitanggang, I. 2016, E&ES, 31, 012012
Rubanenko, L., Venkatraman, J., & Paige, D. A. 2019, NatGe, 12, 597
Sihvola, A., & Sharma, R. 1999, MiOTL, 22, 229
Slade, M. A., Butler, B. J., & Muhleman, D. O. 1992, Sci, 258, 635
Spencer, J. R. 1987, Icar, 70, 99
Sultan-Salem, A. K., & Tyler, G. L. 2006, JGRE, 111, E06S07
Susorney, H. C. M., James, P. B., Johnson, C. L., et al. 2019, Icar, 323, 40
Thompson, T. W., Ustinov, E. A., & Heggy, E. 2011, JGRE, 116, E01006
Thompson, W. R., & Squyres, S. W. 1990, Icar, 86, 336
Vasavada, A. R., Paige, D. A., & Wood, S. E. 1999, Icar, 141, 179
Virkki, A., & Muinonen, K. 2016, Icar, 269, 38
Virkki, A. K., & Bhiravarasu, S. S. 2019, JGRE, 124, 3025
Zuber, M. T., Smith, D. E., Phillips, R. J., et al. 2012, Sci, 336, 217